



## 1    **LABORATORY EXPERIMENTAL INVESTIGATION OF HEAT TRANSPORT IN** 2    **FRACTURED MEDIA**

3    Claudia Cherubini (1) (2), Nicola Pastore (3), Concetta I. Giasi (3), Nicoletta Maria Allegretti (3)

4    (1) Department of Mechanical, Aerospace & Civil Engineering - Brunel University London,  
5    Uxbridge, UB8 3PH, United Kingdom (2) School of Civil Engineering, The University of  
6    Queensland, Queensland, Australia (3) DICATECh - Department of Civil, Environmental, Building  
7    Engineering, and Chemistry – Politecnico di Bari, Italy

8    The authors declares that there is no conflict of interest regarding the publication of this paper.

### 9    **Abstract**

10    Low enthalpy geothermal energy is a renewable resource that is still underexploited nowadays, in  
11    relation to its potential for development in the society worldwide. Most of its applicabilities have  
12    already been investigated, such as: heating and cooling of private and public buildings, roads defrost,  
13    cooling of industrial processes, food drying systems, desalination.

14    One of the major limitations related to the choice of installing low enthalpy geothermal power plants  
15    regards the initial investment costs.

16    In order to increase the optimal efficiency of installations which use groundwater as geothermal  
17    resource, flow and heat transport dynamics in aquifers need to be well characterized. Especially in  
18    fractured rock aquifers these processes represent critical elements that are not well known. Therefore  
19    there is a tendency to oversize geothermal plants.

20    In literature there are very few studies on heat transport especially in fractured media.

21    This study is aimed to deepen the understanding of this topic through heat transport experiments in  
22    fractured network and their interpretation.

23    The heat transfer tests have been carried out on the experimental apparatus previously employed to  
24    perform flow and tracer transport experiments, which has been modified in order to analyze heat  
25    transport dynamics in a network of fractures. In order to model the obtained thermal breakthrough  
26    curves, the Explicit Network Model (ENM) has been used, which is based on an adaptation of a  
27    Tang's solution for the transport of the solutes in a semi-infinite single fracture embedded in a porous  
28    matrix.

29    Parameter estimation, time moment analysis, tailing character and other dimensionless parameters  
30    have permitted to better understand the dynamics of heat transport and the efficiency of heat exchange



between the fractures and matrix. The results have been compared with the previous experimental studies on solute transport.

## Introduction

An important role in transport of natural resources or contaminant transport through subsurface systems is given by fractured rocks. The interest about the study of dynamics of heat transport in fractured media has grown in recent years because of the development of a wide range of applications, including geothermal energy harvesting (Gísladóttir et al., 2016).

Quantitative geothermal reservoir characterization using tracers is based on different approaches for predicting thermal breakthrough curves in fractured reservoirs (Shook, 2001, Kocabas, 2005, Read et al. 2013).

The characterization and modeling of heat transfer in fractured media is particularly challenging as open and well-connected fractures can induce highly localized pathways which are orders of magnitude more permeable than the rock matrix (Klepikova et al, 2016, Cherubini and Pastore, 2011). The study of solute transport in fractured media has become recently a widely diffused research topic in hydrogeology (Cherubini, 2008, Cherubini et al., 2008, Cherubini et al., 2009, Masciopinto et al., 2010), whereas the literature about heat transfer in fractured media is somewhat limited.

Hao et al. (2013) developed a dual continuum model for the representation of discrete fractures and the interaction with surrounding rock matrix in order to give a reliable prediction of the impacts of fracture – matrix interaction on heat transfer in fractured geothermal formations.

Moonen et al. (2011) introduced the concept of cohesive zone which represents a transition zone between the fracture and undamaged material. They proposed a model to adequately represent the influences of fractures or partially damaged material interfaces on heat transfer phenomena.

Geiger and Emmanuel (2010) found that matrix permeability plays an important role on thermal retardations and attenuation of thermal signal. At high matrix permeability, poorly connected fractures can contribute to the heat transport, resulting in heterogeneous heat distributions in the whole matrix block. For lower matrix permeability heat transport occurs mainly through fractures that form a fully connected pathway between the inflow and outflow boundaries, that results in highly non – Fourier behavior, characterized by early breakthrough and long tailing.

Numerous field observations (Tsang and Neretnieks, 1998) show that flow in fractures is being organized in channels due to the small scale variations in the fracture aperture. Flow channeling causes dispersion in fractures. Such channels will have a strong influence on the transport characteristics of a fracture, such as, for instance, its thermal exchange area, crucial for geothermal



63 applications (Auradou et al., 2006). Highly channelized flow in fractured geologic systems has been  
64 credited with early thermal breakthrough and poor performance of geothermal circulation systems  
65 (Hawkins et al., 2012).

66 Lu et. Al (2012) conducted experiments of saturated water flow and heat transfer in a regularly  
67 fractured granite at meter scale. The experiments indicated that the heat advection due to water flow  
68 in vertical fractures nearest to the heat sources played a major role in influencing the spatial  
69 distributions and temporal variations of the temperature, impeding the heat conduction in transverse  
70 direction; such effect increased with larger water fluxes in the fractures and decreased with higher  
71 heat source and/or larger distance of the fracture from the heat source.

72 Neuville et al. (2010) showed that fracture – matrix thermal exchange is highly affected by the  
73 fracture wall roughness. Natarajan et. al (2010) conducted numerical simulation of thermal transport  
74 in a sinusoidal fracture matrix coupled system. They affirmed that this model presents a different  
75 behavior respect to the classical parallel plate fracture matrix coupled system. The sinusoidal  
76 curvature of the fracture provides high thermal diffusion into the rock matrix.

77 Ouyang (2014) developed a three – equation local thermal non – equilibrium model to predict the  
78 effective solid – to – fluid heat transfer coefficient in the geothermal system reservoirs. They affirmed  
79 that due to the high rock – to – fracture size ratio, the solid thermal resistance effect in the internal  
80 rocks cannot be neglected in the effective solid – to fluid heat transfer coefficient. Furthermore the  
81 results of this study show that it is not efficient to extract the thermal energy from the rocks if fracture  
82 density is not large enough.

83 Analytical and semi-analytical approaches have been developed to describe the dynamics of heat  
84 transfer in fractured rocks. Such approaches are amenable to the same mathematical treatment as their  
85 counterparts developed for mass transport (Martinez et al., 2014). One of these is the analytical  
86 solution derived by Tang et al. (1981).

87 While the equations of solute and thermal transport have the same basic form, the fundamental  
88 difference between mass and heat transport is that: 1) solutes are transported through the fractures  
89 only, whereas heat is transported through both fractures and matrix, 2) the fracture-matrix exchange  
90 is large compared with molecular diffusion. This means that the fracture matrix exchange is more  
91 relevant for heat transport than for mass transport. Thus, matrix thermal diffusivity strongly  
92 influences the thermal breakthrough curves (BTCs) (Becker and Shapiro, 2003).



93 Contrarily, since the heat capacity of the solids will retard the advance of the thermal front, the  
94 advective transport for heat is slower than for solute transport (Rau et al., 2012).

95 The quantification of thermal dispersivity as far as heat transport and its relationship with velocity  
96 hasn't been properly addressed experimentally and has got conflicting descriptions in literature (Ma  
97 et al, 2012).

98 Most studies neglect the hydrodynamic component of thermal dispersion because of thermal diffusion  
99 being more efficient than molecular diffusion by several orders of magnitude (Bear 1972). Analysis  
100 of heat transport under natural gradients has commonly neglected hydrodynamic dispersion (e.g.,  
101 Bredehoeft and Papadopoulos 1965; Domenico and Palciauskas 1973; Taniguchi et al. 1999; Reiter  
102 2001; Ferguson et al. 2006). Dispersive heat transport is often assumed to be represented by thermal  
103 conductivity and/or to have little influence in models of relatively large systems and modest fluid  
104 flow rates (Bear, 1972, Woodbury and Smith, 1985).

105 Some authors suggest that thermal dispersivity enhances the spreading of thermal energy and should  
106 therefore be part of the mathematical description of heat transfer in analogy to solute dispersivity (de  
107 Marsily, 1986) and have incorporated this term into their models (e.g., Smith and Chapman, 1983;  
108 Hopmans et al., 2002; Niswonger and Prudic, 2003). In the same way, other researchers (e.g. , Smith  
109 and Chapman, 1983, Ronan et al., 1998, Constantz et al., 2002, Su et al., 2004) have included the  
110 thermomechanical dispersion tensor representing mechanical mixing caused by unspecified  
111 heterogeneities within the porous medium.

112 On the contrary, some other researchers argue that the enhanced thermal spreading is either negligible  
113 or can be described simply by increasing the effective diffusivity, thus the hydrodynamic dispersivity  
114 mechanism is inappropriate. (Bear, 1972; Bravo et al., 2002, Ingebritsen and Sanford, 1998, Keery et  
115 al, 2007). Constantz et al. (2003) and Vandenbohede et al. (2009) found that thermal dispersivity was  
116 significantly smaller than the solute dispersivity. Others (de Marsily, 1986, Molina-Giraldo et al.,  
117 2011) found that thermal and solute dispersivity were on the same order of magnitude.

118 Tracer tests of both solute and heat were carried out at Bonnaud, Jura, France (deMarsily 1986) and  
119 the thermal dispersivity and solute dispersivity were found of the same order of magnitude.

120 Bear (1972), Ingebritsen and Sanford (1998), and Hopmans et al. (2002), among others, concluded  
121 that the effects of thermal dispersion are negligible compared to conduction and set the former to  
122 zero.



123 However, Hopmans et al (2002) showed that dispersivity is increasingly important at higher flow  
124 water velocities, since it is only then that the thermal dispersion term is of the same order of magnitude  
125 or larger than the conductive term.

126 Sauty et al. (1982) suggested that there was a correlation between the apparent thermal conductivity  
127 and Darcy velocity thus they included the hydrodynamic dispersion term in the advective-conductive  
128 modeling.

129 Other similar formulations of this concept are present in the literature (e.g., Papadopoulos and Larson  
130 1978; Smith and Chapman 1983; Molson et al. 1992). Such treatments have not explicitly  
131 distinguished between macrodispersion, which occurs due to variations in permeability over larger  
132 scales and the components of hydrodynamic dispersion that occur due to variations in velocity at the  
133 pore scale.

134 One group of authors have utilized a linear relationship to describe the thermal dispersivity and the  
135 relationship between thermal dispersivity and fluid velocity (e.g., de Marsily, 1986; Anderson, 2005;  
136 Hatch et al., 2006; Keery et al., 2007; Vandenbohede et al., 2009; Vandenbohede and Lebbe, 2010;  
137 Rau et al., 2010), while others have identified the possibility of a nonlinear relationship (Green et al.,  
138 1964).

139 In previous studies by Cherubini et al. (2012, 2013a, 2013b, 2013c and 2014) the presence of  
140 nonlinear flow and non – Fickian transport in a fractured rock formation has been detected. The  
141 experimental results showed evidence of a non-Darcy relationship between hydraulic head  
142 differences and flow rate that is best described by a Forchheimer law.

143 Between the Forchheimer terms and the tortuosity factor a power law has been detected, which means  
144 that the latter influences flow dynamics. Tracer tests were performed to analyse the non - Fickian  
145 nature of transport.

146 The 2 – D Explicit Network Model (ENM) has provided the best fit of the observed experimental  
147 solute BTCs. This approach depicts the fractures as 1-D pipe elements forming a 2-D pipe network  
148 and therefore expressly takes the fracture network geometry into account. The ENM model permits  
149 to understand the physical meaning of flow and transport phenomena and therefore to obtain a more  
150 accurate estimation of flow and transport parameters.

151 In this study, in order to investigate the behavior of heat transport in a fractured network, thermal  
152 tracer tests have been carried out on the same artificially created fractured rock sample.



153 A better development of the Explicit Network Model (ENM) based on a Tang's solution developed  
 154 for solute transport in a single semi-infinite fracture inside a porous matrix has been used for the  
 155 fitting of the thermal BTCs.

156 In analogous way the ENM model has been used in order to fit the observed BTCs obtained from  
 157 previous experiments on mass transport. The obtained thermal BTCs show a more enhanced early  
 158 arrival and long tailing than solute BTCs.

159 The travel time for solute transport is an order of magnitude lower than for heat transport experiments.  
 160 Thermal convective velocity is thus more delayed respect to solute transport. The thermal dispersion  
 161 mechanism dominates heat propagation in the fractured medium in the carried out experiments and  
 162 thus cannot be neglected.

163 For mass transport the presence of the secondary path and the nonlinear flow regime are the main  
 164 factors affecting non – Fickian behavior observed in experimental BTCs, whereas for heat transport  
 165 non - Fickian nature of the experimental BTCs is governed mainly by the heat exchange mechanism  
 166 between the fracture network and the surrounding matrix. The presence of a nonlinear flow regime  
 167 gives rise to a weak growth on heat transfer phenomena.

168 Furthermore the estimation of the average effective thermal conductivity suggests that there is a solid  
 169 thermal resistance in the fluid to solid heat transfer processes due to the rock – fracture size ratio.  
 170 This result matches previous analyses (Pastore et al., 2015) in which a lower heat dissipation respect  
 171 to the Tang's solution in correspondence of the single fracture surrounded by a matrix with more  
 172 limited heat capacity has been found.

## 173 **Theoretical background**

### 174 **Nonlinear flow**

175 With few exceptions, any fracture can be envisioned as two rough surfaces in contact. In cross  
 176 section the solid areas representing asperities might be considered as the grains of porous media.

177 Therefore, in most studies examining hydrodynamic processes in fractured media, the general  
 178 equations describing flow and transport in porous media are applied, such as Darcy's law, that depicts  
 179 a linear relationship between the pressure gradient and fluid velocity (Whitaker, 1986; Cherubini and  
 180 Pastore, 2010a)

181 However, this linearity has been demonstrated to be valid at low flow regimes ( $Re < 1$ ). For  $Re > 1$  a  
 182 nonlinear flow behavior is likely to occur (Cherubini, 2013d).



183 When  $Re \gg 1$ , a strong inertial regime develops, that can be described by the Forchheimer equation  
 184 (Forchheimer, 1901):

$$185 \quad -\frac{dp}{dx} = \frac{\mu}{k} \cdot u_f + \rho\beta \cdot u_f^2 \quad (1)$$

186 Where  $\beta$  ( $L^{-1}$ ) is called the inertial resistance coefficient, or non – Darcy coefficient.

187 It is possible to express Forchheimer law in terms of hydraulic head:

$$188 \quad -\frac{dh}{dx} = a' \cdot u_f + b' \cdot u_f^2 \quad (2)$$

189 The coefficients  $a$  ( $TL^{-1}$ ) and  $b$  ( $TL^{-2}$ ) represent the linear and inertial coefficient respectively equal  
 190 to:

$$191 \quad a' = \frac{\mu}{\rho g k}; \quad b' = \frac{\beta}{g} \quad (3)$$

192 The relationship between hydraulic head gradient and flow rate  $Q$  ( $L^3T^{-1}$ ) can be written as:

$$193 \quad -\frac{dh}{dx} = a \cdot Q + b \cdot Q^2 \quad (4)$$

194 The coefficients  $a$  ( $TL^{-3}$ ) and  $b$  ( $T^2L^{-6}$ ) can be related to  $a'$  and  $b'$ :

$$195 \quad a = \frac{a'}{\omega_{eq}}; \quad b = \frac{b'}{\omega_{eq}} \quad (5)$$

196 Where  $\omega_{eq}$  ( $L^2$ ) is the equivalent cross sectional area of fracture.

#### 197 **Heat transfer by water flow in single fractures**

198 Fluid flow and heat transfer in a single fracture ( $SF$ ) undergo advective, diffusive and dispersive  
 199 phenomena. Dispersion is caused by small scale fracture aperture variations. Flow channeling is one  
 200 example of macrodispersion caused by preferred flow paths, in that mass and heat tend to migrate  
 201 through the portions of a fracture with the largest apertures.

202 In fractured media another process is represented by diffusion into surrounding rock matrix. Matrix  
 203 diffusion attenuates the mass and heat propagation in the fractures.

204 According to the boundary – layer theory (Fahien, 1983), solute mass transfer  $q_m$  ( $ML^{-2}$ ) per unit area  
 205 at the fracture-matrix interface (Wu et al., 2010) is given by:



$$q_M = \frac{D_m}{\delta} (c_f - c_m) \quad (6)$$

Where  $c_f$  ( $\text{ML}^{-3}$ ) is the concentration across fractures,  $c_m$  ( $\text{ML}^{-3}$ ) is the concentration of the matrix block surfaces,  $D_m$  ( $\text{LT}^{-2}$ ) is the molecular diffusion coefficient, and  $\delta$  (m) is the thickness of boundary layer (Wu et al., 2010). For small fractures,  $\delta$  may become the aperture  $w_f$  (m) of the SF.

In analogous manner the specific heat transfer flux  $q_H$  ( $\text{MT}^{-3}$ ) at the fracture – matrix interface is given by:

$$q_H = \frac{k_m}{\delta} (T_f - T_m) \quad (7)$$

Where  $T_f$  (K) is the temperature across fractures,  $T_m$  (K) is the temperature of the matrix block surfaces,  $k_m$  ( $\text{MLT}^{-3}\text{K}^{-1}$ ) is the thermal conductivity.

The continuity conditions at the fracture – matrix interface requires a balance between mass transfer rate and mass diffused into the matrix described as:

$$q_M = -D_e \left. \frac{\partial C_m}{\partial z} \right|_{z=w_f/2} \quad (8)$$

Where  $z$  (m) is the coordinate perpendicular to the fracture axis and  $w_f$  is the aperture of the fracture.

In the same way the specific heat flux must be balanced by heat diffused into the matrix described as:

$$q_H = -k_e \left. \frac{\partial T_m}{\partial z} \right|_{z=w_f/2} \quad (9)$$

The effective terms ( $D_e$  instead of  $D_m$  and  $k_e$  instead of  $k_m$ ) have been introduced in order to include the effect of various system parameters such as fluid velocity, porosity, surface area, roughness, that may enhance mass and heat transfer effect. For instance, when large flow velocity occurs, convective transport is stronger along the centre of the fracture, enhancing the concentration or temperature gradient at the fracture matrix interface. As known roughness plays an important role in increasing mass or heat transfer because of increasing turbulent flow conditions.

According to Bodin (2007) the governing equation for the one dimensional advective - dispersive transport along the axis of a semi-infinite fracture with one – dimensional diffusion in the rock matrix, in perpendicular direction to the axis of the fracture is:





$$230 \quad \frac{\partial c_f}{\partial t} + u_f \frac{\partial c_f}{\partial x} = \frac{\partial}{\partial x} \left( D_f \frac{\partial c_f}{\partial x} \right) - \frac{D_e}{\delta} \frac{\partial c_m}{\partial z} \Big|_{z=w_f/2} \quad (10)$$

231 Where  $x$  (m) is the coordinate parallel to the axis of  $SF$ ,  $u_f$  ( $LT^{-1}$ ) is the convective velocity,  $D_f$  ( $L^2T^{-1}$ )  
 232 is the dispersion coefficient. The latter mainly depends on two processes: Aris – Taylor dispersion  
 233 and geometrical dispersion. Previous experiments (Cherubini et al., 2013) show that, due to the  
 234 complex geometrical and topological characteristics of the fracture network that create tortuous flow  
 235 paths, Aris – Taylor dispersion may not develop. A linear relationship has been found between  
 236 velocity and dispersion so geometrical dispersion is mostly responsible for the mixing process along  
 237 the fracture:

$$238 \quad D_f = \alpha_{LM} u_f \quad (11)$$

239 Where  $\alpha_{LM}$  (L) is the dispersion coefficient for mass transport.

240 Assuming that fluid flow velocity in the surrounding rock matrix is equal to zero, the equation for the  
 241 conservation of heat in the matrix is given by:

$$242 \quad \frac{\partial C_m}{\partial t} = D_a \frac{\partial^2 C_m}{\partial z^2} \quad (12)$$

243 Where  $D_a$  is the apparent diffusion coefficient of the solute in the matrix expressed as function of  $\theta_m$   
 244 (-) the matrix porosity  $D_a = D_e / \theta_m$  (Bodin et al., 2007). Tang et al. (1981) presented an analytical  
 245 solution for solute transport in semi – infinite single fracture embedded in a porous rock matrix with  
 246 a constant concentration at the fracture inlet ( $x=0$ ) equal to  $c_0$  ( $ML^{-3}$ ) and with an initial concentration  
 247 equal to zero. The solute concentration in the fracture  $\bar{c}_f$  and in the matrix  $\bar{c}_m$  has been given as  
 248 function of time in Laplace space.

$$249 \quad \bar{c}_f = \frac{c_0}{s} \exp(vL) \exp \left[ -vL \left\{ 1 + \beta^2 \left( \frac{s^{1/2}}{A} + s \right) \right\}^{1/2} \right] \quad (13)$$

$$250 \quad \bar{c}_m = \bar{c}_f \exp \left[ -Bs^{1/2} \left( z - w_f / 2 \right) \right] \quad (14)$$

251 Whereas the gradient of  $\bar{c}_m$  at the interface  $z = w_f/2$  is:



$$\left. \frac{d\bar{c}_m}{dx} \right|_{x=w_f/2} = -\bar{c}_f B s^{1/2} \quad (15)$$

The  $\nu$ ,  $A$ ,  $\beta^2$  and  $B$  coefficients are expressed as follows:

$$\nu = \frac{u_f}{2D_f} \quad (16)$$

$$A = \frac{\delta}{\sqrt{\theta D_e}}; \quad \theta = \theta_m \quad (17)$$

$$\beta^2 = \frac{4D_f}{u_f^2} \quad (18)$$

$$B = \frac{1}{\sqrt{D_e}} \quad (19)$$

Furthermore on the basis of these analytical solutions the probability density function of the solute residence time (*PDF*) in the single fracture in the Laplace space can be expressed as:

$$\bar{\Gamma}(s) = \exp(\nu L) \exp \left[ -\nu L \left\{ 1 + \beta^2 \left( \frac{s^{1/2}}{A} + s \right) \right\}^{1/2} \right] \quad (20)$$

Assuming that density and heat capacity are constant in time, the heat transport conservation equation in *SF* can be expressed as follows:

$$\frac{\partial T_f}{\partial t} + u_f \frac{\partial T_f}{\partial x} = \frac{\partial}{\partial x} \left( D_{fh} \frac{\partial T_f}{\partial x} \right) - \frac{k_e}{\rho_w C_w \delta} \frac{\partial T_m}{\partial z} \bigg|_{z=w_f/2} \quad (21)$$

Where  $\rho_w$  ( $\text{ML}^{-3}$ ),  $C_w$  ( $\text{L}^2\text{T}^2\text{K}^{-1}$ ) represent the density, the specific heat capacity of the fluid within *SF* respectively.  $D_f$  for heat transport assumes the following expressions:

$$D_{fh} = \frac{\lambda_L}{\rho_w C_w} \quad (22)$$

Where  $\lambda_L$  is the thermodynamic dispersion coefficient ( $\text{MLT}^{-3}\text{K}^{-1}$ ). Sauty et al. (1982) and de Marsily (1986) proposed an expression for the thermal dispersion coefficient where the thermal dispersion term varies linearly with velocity and depends on the heterogeneity of the medium, as for solute transport:



$$\lambda_L = k_0 + \alpha_{LH} \rho_w c_w u_f \quad (23)$$

Where  $k_0$  is the bulk thermal conductivity ( $\text{MLT}^{-3}\text{K}^{-1}$ )  $\alpha_{LH}$  (L) is the longitudinal thermal dispersivity.

The heat transport conservation equation in the matrix is expressed as follows:

$$\rho_m C_m \frac{\partial T_m}{\partial t} = k_e \frac{\partial^2 T_m}{\partial z^2} \quad (24)$$

Note that the governing equations of heat and mass transport highlight similarities between the two processes, thus Tang's solution can be used also for heat transport.

In terms of heat transport, the coefficients  $v$ ,  $A$ ,  $\beta^2$  and  $B$  are expressed as follows:

$$v = \frac{u_f}{2D_{fH}}; \quad (25)$$

$$A = \frac{\delta}{\sqrt{\theta D_e}}; \quad \theta = \frac{\rho_m C_m}{\rho_f C_f}, \quad D_e = \frac{k_e}{\rho_w C_w} \quad (26)$$

$$\beta^2 = \frac{4D_f}{u_f^2} \quad (27)$$

$$B = \frac{1}{\sqrt{D_e}} \quad (28)$$

Three characteristic time scales can be defined:

$$t_u = \frac{L}{u_f}; \quad t_d = \frac{L^2}{D_f}; \quad t_e = \frac{\delta^2}{D_e} \quad (29)$$

Where  $L$  (L) is the characteristic length,  $t_u$  (T),  $t_d$  (T) and  $t_e$  (T) represent the characteristics time scales of convective transport, dispersive transport and loss of the mass or heat into the surrounding matrix.

The relative effect of dispersion, convection and matrix diffusion on mass or heat propagation in the fracture can be evaluated by comparing the correspondent time scale.

Peclet number  $Pe$  is defined as the ratio between convective to dispersive transport times:

$$Pe = \frac{t_d}{t_u} = \frac{u_f L}{D_f} \quad (30)$$



290 At high Peclet numbers transport processes are mainly governed by convection, whereas at low Peclet  
 291 numbers it is mainly dispersion that dominates.

292 Another useful dimensionless number, generally applied in chemical engineering, is the Damköhler  
 293 number that can be used in order to evaluate the influence of matrix diffusion on convection  
 294 phenomena. The Damköhler number is based on the exchange rate coefficient corresponding to:

$$295 \quad \alpha = \frac{D_e}{\delta^2} \quad (31)$$

296 Note that the inverse of  $t_e$  has the same meaning of the exchange rate coefficient  $\alpha$  ( $T^{-1}$ ).  $Da$  relates  
 297 the convection time scale to the exchange time scale.

$$298 \quad Da = \frac{t_u}{t_e} = \frac{\alpha L}{u_f} \quad (32)$$

299 When  $t_e$  values are of the same order of magnitude as the transport time  $t_u$  ( $Da \cong 1$ ), diffusive  
 300 processes in the matrix are more relevant. In this case concentration or temperature distribution  
 301 profiles are characterized by a long tail.

302 When  $t_e \gg t_u$  ( $Da \ll 1$ ) the fracture – matrix exchange is very slow and it does not influence mass  
 303 or heat propagation. On the contrary when  $t_e \ll t_u$  ( $Da \gg 1$ ) the fracture matrix exchange is rapid,  
 304 there is instantaneous equilibrium between fracture and matrix and they have the same concentration  
 305 or temperature. These two circumstances close the standard advective – dispersive transport equation.

306 The product between  $Pe$  and  $Da$  represents another dimensionless group which is a measure of  
 307 transport processes:

$$308 \quad Pe \times Da = \frac{t_d}{t_e} = \frac{\alpha L^2}{D_f} \quad (33)$$

309 When  $Pe \times Da$  increases  $t_e$  decreases more rapidly than  $t_d$ , and subsequently the mass or heat  
 310 diffusion into the matrix may be dominant on the longitudinal dispersion.

### 311 **Explicit network model (ENM)**

312 With the assumption that a  $SF_j$  can be schematized by a 1d – pipe element, the Forchheimer model  
 313 can be used to write the relationship between head loss  $\Delta h_j$  (L) and flow rate  $Q_j$  ( $L^3T^{-1}$ ) in finite  
 314 terms:



$$\frac{\Delta h_j}{L_j} = aQ_j + bQ_j^2 \Rightarrow \Delta h_j = \left[ L_j (a + bQ_j) \right] Q_j \quad (34)$$

Where  $L_j$  (L) is the length of  $SF_j$ ,  $a$  ( $TL^{-3}$ ) and  $b$  ( $T^2L^{-6}$ ) represent the Forchheimer parameters written in finite terms. The term in the square brackets constitutes the resistance to flow  $R_j(Q_j)$  ( $TL^{-2}$ ) of  $SF_j$ .

In case of steady – state conditions and for a simple 2d fracture network geometry, a straightforward manner can be applied to obtain the solution of flow field by applying the first and second Kirchhoff's laws.

In a 2d fracture network, fractures can be arranged in series and/or in parallel. Specifically, in a network in which fractures are set in a chain, the total resistance to flow is calculated by simply adding up the resistance values of each single fracture. The flow in a parallel fracture network breaks up, with some flowing along each parallel branch and re – combining when the branches meet again. In order to estimate the total resistance to flow the reciprocals of the resistance values have to be added up and then the reciprocal of the total has to be calculated. The flow rate  $Q_j$  across the generic fracture  $j$  of the parallel network can be calculated as (Cherubini et al., 2014):

$$Q_j = \sum Q \left[ \frac{1}{R_j} \left( \sum_{i=1}^n \frac{1}{R_i} \right)^{-1} \right] \quad (35)$$

Where  $\sum Q$  ( $LT^{-3}$ ) is the sum of the mass flow rates at fracture intersections in correspondence of the inlet bond of  $j$  fracture, whereas the term in square brackets represents the probability of water distribution of  $j$  fracture  $P_{Qj}$ .

Once known the flow field in the fracture network, to obtain the *PDF* at a generic node the *PDFs* of each elementary path that reaches the node have to be summed up. They can be calculated as the convolution product of the *PDFs* of each single fracture composing the elementary path.

Definitely the BTC describing the concentration in the fracture as function of time at the generic node, using the convolution theorem, can be obtained as follows:

$$c_f(t) = c_0 + c_{inj}(t) * L^{-1} \left[ \sum_{i=1}^{N_p} \prod_{j=1}^{n_{fj}} P_{M,j} \bar{\Gamma}_j(s) \right] \quad (36)$$



Where  $c_0$  ( $\text{ML}^{-3}$ ) is the initial concentration and  $c_{inj}$  ( $\text{ML}^{-3}$ ) is the concentration injection function, (\*) is the convolution operator,  $L^{-1}$  represents the inverse Laplace transform operator,  $N_p$  is the number of the paths that reach the node,  $n_{f,i}$  is the number of the  $SF$  belonging to the elementary path  $i^{\text{th}}$ ,  $P_{M,j}$  and  $\bar{\Gamma}(s)$  are the mass distribution probability and the  $PDF$  in the Laplace space of the generic  $j^{\text{th}}$   $SF$  respectively. Inverse Laplace transform  $L^{-1}$  can be solved numerically using Abate et al. (2006) algorithm.

At the same way the BTC  $T_f$  which describes the temperature in the fracture as function of time at the generic node can be written as:

$$T_f(t) = T_0 + T_{inj}(t) * L^{-1} \left[ \sum_{i=1}^{N_p} \prod_{j=1}^{n_{f,i}} P_{H,j} \bar{\Gamma}_j(s) \right] \quad (37)$$

Where  $T_0$  (K) is the initial temperature and  $T_{inj}$  (K) is the temperature injection function,  $P_{H,j}$  is the heat distribution probability.

$P_{M,j}$  and  $P_{H,j}$  can be estimated as the probabilities of the mass and heat distribution at the inlet bond of each individual  $SF$  respectively. The mass and heat distribution is proportional to the correspondent flow rates:

$$P_{M,j} = P_{H,j} = \frac{Q_j}{\sum Q} \quad (38)$$

Where  $Q_j$  is the flow rate in the  $j$   $SF$  and  $\sum Q$  is the sum of the flow rate calculated at the fracture intersection in correspondence of the inlet bond of  $j$  fracture. Note that if Equation 37 is valid, the probability of water distribution is equal to the probabilities of mass and heat distribution (term in square brackets in Equation 34). Definitely the ENM model regarding each  $SF$  can be described by four parameters ( $u_{f,j}$ ,  $D_{f,j}$ ,  $\alpha_j$ ,  $P_{Q,j}$ ).

## Material and methods

### Description of the experimental apparatus

The heat transfer tests have been carried out on the experimental apparatus previously employed to perform flow and tracer transport experiments at bench scale (Cherubini et al. 2012, 2013a, 2013b, 2013c and 2014). However, the apparatus has been modified in order to analyze heat transport dynamics. Two thermocouples have been placed at the inlet and the outlet of a selected fracture path



of the limestone block with parallelepiped shape ( $0.6 \times 0.4 \times 0.08 \text{ m}^3$ ) described in previous studies. A TC – 08 Thermocouple Data Logger (pico Technology) with a sampling rate of 1 second has been connected to the thermocouples. An extruded polystyrene panel with thermal conductivity equal to  $0.034 \text{ Wm}^{-1}\text{K}^{-1}$  and thickness 0.05 m has been used to thermally insulate the limestone block which has then been connected to a hydraulic circuit. The difference in hydraulic head between the upstream tank connected to the inlet port and the downstream tank connected to the outlet port drives flow of water through the fractured block. An ultrasonic velocimeter (DOP3000 by Signal Processing) has been adopted to measure the instantaneous flow rate that flows across the block. An electric boiler with a volume of  $10^{-2} \text{ m}^3$  has been used to heat the water. In a flow cell located in correspondence of the outlet port a multiparametric probe is positioned for the instantaneous measurement of pressure (dbar), temperature ( $^{\circ}\text{C}$ ) and electric conductivity ( $\mu\text{S cm}^{-1}$ ). The schematic diagram of the experimental apparatus is shown in Figure 1.

#### **Flow experiments.**

The average flow rate through the selected path can be evaluated as:

$$\bar{Q} = \frac{S_l}{t_1 - t_0} (h_1 - h_0) \quad (39)$$

Where  $S_l \text{ (L}^2\text{)}$  is the cross section area of the flow cell,  $\Delta t = t_1 - t_0$  is the time for the flow cell to be filled from  $h_0 \text{ (L)}$  and  $h_1 \text{ (L)}$ . To calculate the average hydraulic head differences between the upstream tank and the flow cell the following expression is adopted:

$$\Delta h = h_c - \frac{h_0 + h_1}{2} \quad (40)$$

Where  $h_c$  is the hydraulic head measured in the upstream tank. Several tests have been carried out varying the control head, and in correspondence of each value of the average flow rate and head differences the average resistance to flow has been determined as:

$$\bar{R}(\bar{Q}) = \left[ \frac{S_l}{t_1 - t_0} \ln \left( \frac{h_0 - h_c}{h_1 - h_c} \right) \right]^{-1} \quad (41)$$

#### **Solute and temperature tracer tests**

Solute and temperature tracer tests have been conducted through the following steps.



390 As initial condition, a specific value of hydraulic head difference between the upstream tank and  
 391 downstream tank has been assigned. At  $t = 0$  the valve  $a$  is closed so as the hydrostatic head inside  
 392 the block assumes the same value to the one in the downstream tank. At  $t = 10$  s the valve  $a$  is opened.

393 For solute tracer test at time  $t = 60$  s by means of a syringe, a mass of  $5 \times 10^{-4}$  kg sodium chloride is  
 394 injected into the inlet port. Due to the very short source release time, the instantaneous source  
 395 assumption can be adopted. The multiparametric probe located within the flow cell measures the  
 396 solute BTC.

397 As concerns thermal tracer tests at the time  $t = 60$  s the valve  $d$  is opened while the valve  $c$  is closed.  
 398 In such a way a step temperature function in correspondence of the inlet port  $T_{inj}(t)$  is imposed and  
 399 measured by the first thermocouple. The other thermocouple located inside the outlet port is used to  
 400 measure the thermal BTC.

401 The ultrasonic velocimeter is used in order to measure the instantaneous flow rate, whereas a  
 402 multiparametric probe located at the outlet port measures the pressure and the electric conductivity.

## 403 **Results and discussion**

### 404 *Flow characteristics*

405 The Kirchhoff laws have been used in order to estimate the flow rates flowing in each single fracture.  
 406 In figure 2 a sketch of the 2d pipe conceptualization of the fracture network is reported.

407 The linear and nonlinear terms have been assumed equal for each single fracture of the fracture  
 408 network and have been estimated matching the average experimental resistance to flow resulting from  
 409 Equation (41) with resistance to flow estimated as:

$$410 \quad \bar{R}(\bar{Q}) = R_1(Q_0) + R_2(Q_0) + \left( \frac{1}{R_6(Q_1)} + \frac{1}{R_3(Q_2) + R_4(Q_2) + R_5(Q_2)} \right)^{-1} +$$

$$+ R_7(Q_0) + R_8(Q_0) + R_9(Q_0) \quad (42)$$

411 The flow rate  $Q_I$  is determined using the following iterative equation:

$$412 \quad Q_1^{k+1} = Q_0 \left[ \frac{R_3(Q_0 - Q_1^k) + R_4(Q_0 - Q_1^k) + R_5(Q_0 - Q_1^k)}{R_3(Q_0 - Q_1^k) + R_4(Q_0 - Q_1^k) + R_5(Q_0 - Q_1^k) + R_6(Q_1^k)} \right] \quad (43)$$

413 Whereas the flow rate  $Q_2$  is determined merely as:

$$414 \quad Q_2 = Q_0 - Q_1 \quad (44)$$





415 The linear and nonlinear term are equal respectively to  $a = 7.345 \times 10^4 \text{ sm}^{-3}$  and  $b = 11.65 \times 10^9 \text{ s}^2 \text{ m}^{-6}$ .  
 416 Inertial forces dominate viscous ones when the Forchheimer number is higher than one. The critical  
 417 flow rate  $Q_{crit}$  can be determined in correspondence of  $Fo = 1$  as the ratio between  $a$  and  $b$  resulting  
 418  $Q_{crit} = 6.30 \times 10^{-6} \text{ m}^3 \text{ s}^{-1}$ .

419 Because of the nonlinearity of flow, varying the inlet flow rate  $Q_0$  the ratio between the flow rates  $Q_1$   
 420 and  $Q_2$  flowing respectively in the branches 6 and 3 – 5 is not constant. When  $Q_0$  increases  $Q_2$   
 421 increases faster than  $Q_1$ . The probability of water distribution of the branch 6  $P_{Q,6}$  is evaluated as the  
 422 ratio between  $Q_0$  and  $Q_1$ , whereas the probability of water distribution of the branch 3 – 5 is equal to  
 423  $P_{Q,3-5} = 1 - P_{Q,6}$ .

#### 424 ***Fitting of breakthrough curves and interpretation of estimated model parameters***

425 The behavior of mass and heat transport has been compared varying the injection flow rates. In  
 426 particular 21 tests in the range  $1.83 \times 10^{-6} - 1.26 \times 10^{-5} \text{ m}^3 \text{ s}^{-1}$  for heat transport have been made and  
 427 compared with the 55 tests in the range  $1.32 \times 10^{-6} - 8.34 \times 10^{-6} \text{ m}^3 \text{ s}^{-1}$  for solute transport presented in  
 428 previous studies.

429 The observed heat and mass BTCs for different flow rates have been individually fitted using the  
 430 ENM approach presented in the previous section. The transport parameters  $u_f$ ,  $D_f$  and  $\alpha$  are assumed  
 431 equal for all branches of the fracture network. The probability of mass and heat distribution are  
 432 assumed equal to the probability of water distribution.

433 The experimental BTCs are fitted using Equation 35 and Equation 36 for mass and heat transport  
 434 respectively. Note that for mass transport  $c_{inj}(t)$  supposing the instantaneous injection condition  
 435 becomes a Dirac delta function.

436 The determination coefficient ( $r^2$ ) and the root mean square error ( $RMSE$ ) have been used in order to  
 437 evaluate the goodness of fit.

438 Tables 1 and 2 show the values of transport parameters, the  $RMSE$  and  $r^2$  for mass and heat transport  
 439 respectively. Furthermore Figure 3 and Figure 4 show the fitting results of BTCs for some values of  
 440  $Q_0$ .

441 The estimated convective velocities  $u_f$  for heat transport are lower than for mass transport. Whereas  
 442 the estimated dispersion coefficients  $D_f$  for heat transport are higher than for mass transport.  
 443 Regarding the transfer rate coefficient  $\alpha$ , it assumes very low values for mass transport relatively to  
 444 the convective velocity. Instead for heat transport the exchange rate coefficient is of the same order



of magnitude of the convective velocity and, considering a characteristic length equal to  $L = 0.601$  m, the effect of dual – porosity is very strong and cannot be neglected relatively to the investigated injection flow range.

Both mass and heat transport show a satisfactory fitting. In particular manner,  $RMSE$  varies in the range  $0.0015 - 0.0180$  for mass transport and in the range  $0.0030 - 0.236$  for heat transport, whereas  $r^2$  varies in the range  $0.9863 - 0.9987$  for mass transport and in the range  $0.0963 - 0.9998$  for heat transport.

In order to investigate the different behavior between mass and heat transport, the relationships between injection flow rate and the transport parameters have been analyzed. In Figure 5 the relationship between  $u_f$  and  $Q_0$  is reported. Whereas in figures 6 and 7 are reported the dispersion coefficient  $D_f$  and the exchange term  $\alpha$  as function of  $u_f$ . The figures show a very different behavior between mass and heat transport.

Regarding mass transport experiments according to previous studies (Cherubini et al., 2013 and 2014) the figure 5 shows that for values of  $Q_0$  higher than  $4 \times 10^{-6} \text{ m}^3 \text{ s}^{-1}$   $u_f$  increases less rapidly. This behavior was due to the presence of inertial forces that gave rise to a retardation effect on solute transport.

Instead figure 6 shows a linear relationship between  $u_f$  and  $D_f$  suggesting that inertial forces didn't exert any effect on dispersion and that geometrical dispersion dominates the Aris – Taylor dispersion.

The estimated exchange rate coefficient  $\alpha$  is much lower than the convective velocity. These results suggest that in the case study fracture – matrix exchange is very slow and it may not influence mass transport. Non Fickian behavior observed in the experimental BTCs is therefore dominated mainly by the presence of inertial forces and the parallel branches.

A very different behavior is observed for heat transport. Heat convective velocity doesn't seem to be influenced by the presence of the inertial force whereas  $u_f$  is influenced by fracture matrix exchange phenomena resulting in a significant retardation effect.

In the same way as for mass transport, for heat transfer a linear relationship is evident between dispersion and convective velocity. Even if heat convective velocity is lower than solute advective velocity, the longitudinal thermal dispersivity assumes higher values than the longitudinal solute dispersivity. Also for heat transport experiments a linear relationship between  $u_f$  and  $D_f$  has been found.



475 Once the model parameters for each flow rate have been determined, the unit response function ( $f_{URF}$ ),  
 476 corresponding to the *PDF* obtained from impulsive injection of both solute and temperature tracers,  
 477 is obtained. The unit response function can be characterized using the time moments and tail character  
 478 analysis.

479 The mean residence time  $t_m$  assumes the following expression:

$$480 \quad t_m = \frac{\int_0^{\infty} t f_{URF}(t) dt}{\int_0^{\infty} f_{URF}(t) dt} \quad (45)$$

481 Whereas the  $n^{\text{th}}$  normalized central moment of distribution of the  $f_{URF}$  versus time can be written as:

$$482 \quad \mu_n = \frac{\int_0^{\infty} (t - t_m)^n f_{URF}(t) dt}{\int_0^{\infty} f_{URF}(t) dt} \quad (46)$$

483 The second moment  $\mu_2$  can be used in order to evaluate the dispersion relative to  $t_m$ , whereas the  
 484 skewness is a measure of the degree of asymmetry and it is defined as follows:

$$485 \quad S = \mu_3 / \mu_2^{3/2} \quad (47)$$

486 The tailing character  $t_c$  can be described as:

$$487 \quad t_c = \frac{\Delta t_{fall}}{\Delta t_{rise}} \quad (48)$$

488 Where  $\Delta t_{fall}$  denotes the duration of the falling limb defined as the time interval from the peak to the  
 489 tail cutoff which is the time when the falling limb first reaches a value that is 0.05 times the peak  
 490 value.  $\Delta t_{rise}$  is defined as the time interval from the first arrival to the peak. This quantity provides a  
 491 measure of the asymmetry between the rising and falling limbs. A value of  $t_c$  significantly higher than  
 492 1 indicates an elongated tail compared to the rising limb (Cherubini et al., 2010b).

493 In Figure 8 is reported the mean travel time versus the injection flow rates. The figure highlights that  
 494  $t_m$  for heat transport is about 3 times higher than for mass transport. In particular way  $t_m$  varies in the  
 495 range 40.3 - 237.1 s for mass transport and in the range 147.8 - 506.9 s for heat transport. This result  
 496 still highlights that heat transport is more delayed than mass transport.

497 In same way the skewness  $S$  (Figure 9) and tailing character  $t_c$  (Figure 10) are reported as function of  
 498  $Q_0$ .



499 A different behavior for heat and mass transport is observed for the skewness coefficient. For heat  
 500 transfer the skewness shows a growth trend which seems to decrease after  $Q_0 = 3 \times 10^{-6} \text{ m}^3 \text{ s}^{-1}$ . Its mean  
 501 value is equal to 2.714. For solute transport the  $S$  does not show a trend, and assumes a mean value  
 502 equal to 2.018.

503 The tailing character does not exhibit a trend for both mass and heat transport. In either cases  $t_c$  is  
 504 significantly higher than 1, specifically 7.70 and 30.99 for mass and heat transport respectively.

505 In order to explain the transport dynamics, the trends of dimensionless numbers  $Pe$  and  $Da$  varying  
 506 the injection flow rate have been investigated. The Figure 11 shows the  $Pe$  as function of  $Q_0$  for both  
 507 mass and heat experiments. As concerns mass experiments  $Pe$  increases as  $Q_0$  increases, assuming a  
 508 constant value for high values ( $Pe = 7.5$ ) of  $Q_0$ . For heat transport a different behavior is observed,  
 509  $Pe$  showing a constant trend and being always lower than one. Even if the injection flow rate is  
 510 relatively high, thermal dispersion is the dominating mechanism in heat transfer.

511 Figure 12 reports  $Da$  as function of  $Q_0$ . For mass transport  $Da$  assumes very low values, of the order  
 512 of magnitude of  $10^{-4}$ .

513 The convective transport scale is very low respect to the exchange transport scale, thus the mass  
 514 transport in each single fracture can be represented with the classical advection dispersion model.

515 As regards heat transport  $Da$  assumes values around the unit showing a downward trend as injection  
 516 flow rate increases switching from higher to lower values than the unit. As injection flow rate  
 517 increases the convective transport time scale reduces more rapidly than the exchange time scale.

518 These arguments can be explained because the relationships between  $Q_0$  and  $u_f$  show a change of  
 519 slope when  $Da$  becomes lower than the unit. In other words when  $Da$  is higher than the unit the  
 520 exchange between fracture and matrix dominates on the convective transport giving rise to a more  
 521 enhanced delay on heat transport, conversely when  $Da$  is lower than one convective transport  
 522 dominates on fracture- matrix interactions and the delay effect is reduced.

523 Furthermore this effect is evident also on the trend observed in the graph  $S - Q_0$  (Figure 9). For values  
 524 of  $Da$  lower than the unit a change of slope is evident, the skewness coefficient increases more slowly.  
 525 Thus for  $Da > 1$  the early arrival and the tail effect of  $BTC$  increase more rapidly than for  $Da < 1$ .

526 Note that even if  $Da$  presents a downward trend as  $Q_0$  increases, when the latter exceeds  $Q_{crit}$  a weak  
 527 growth trend for  $Da$  is detected, that however assumes values lower than the unit.



528 The Figure 13 shows the dimensionless group  $Pe \times Da$  varying the injection flow rate. Regarding mass  
 529 transport  $Pe \times Da$  is of the order of magnitude of  $10^{-3}$  confirming the fact that the fracture – matrix  
 530 interaction can be neglected relatively to the investigated range of injection flow rates. For heat  
 531 transport  $Pe \times Da$  assumes values just below the unit, with a downward trend as  $Q_0$  increases.  $t_d$  and  $t_e$   
 532 have the same order of magnitude.

533 In order to find the optimal conditions for heat transfer in the analyzed fractured medium the thermal  
 534 power exchanged per unit temperature difference  $\dot{Q}/(T_{inj} - T_0)$  ( $ML^2T^{-1}K^{-1}$ ) for each injection flow rate  
 535 in quasi steady state conditions can be estimated. The thermal power exchanged can be written as:

$$536 \quad \dot{Q} = \rho C_p Q_0 (T_{inj} - T_{out}) \quad (49)$$

537 The outlet temperature  $T_{out}$  can be evaluated as function of the  $f_{URF}$  using the following expression:

$$538 \quad T_{out} = T_0 + (T_{inj} - T_0) \int_0^\infty f_{URF}(t) dt \quad (50)$$

539 Substituting the Equation (50) in the Equation (49) the thermal power exchanged per unit temperature  
 540 difference is:

$$541 \quad \frac{\dot{Q}}{(T_{inj} - T_0)} = \left(1 - \int_0^\infty f_{URF}(t) dt\right) \rho C_p Q_0 \quad (51)$$

542 Figure 14 shows the similarities between the relationship  $\dot{Q}/(T_{inj} - T_0) - Q_0$  (Figure 14 a) and  $Da - Q_0$   
 543 (Figure 14 b). Higher  $Da$  values correspond to higher values of  $\dot{Q}/(T_{inj} - T_0)$ . The thermal power  
 544 exchanged increases as the Damköhler number increases as shown in Figure 14c. These results  
 545 highlight that for the observed case study the optimal condition for thermal exchange in the fractured  
 546 medium is obtained when the exchange time scale is lower than the convective transport scale or  
 547 rather when the dynamics of fracture – matrix exchange are dominant on the convective ones.

548 Moreover in a similar way to  $Da$ ,  $\dot{Q}/(T_{inj} - T_0)$  shows a weak growth trend when  $Q_0$  exceeds  $Q_{crit}$ . This  
 549 means that the nonlinear flow regime improves the fracture – matrix thermal exchange, however at  
 550 high values of injection flow rates convective and dispersion time scales are less than the exchange  
 551 time scale. Nevertheless these results have been observed in a small range of  $Da$  numbers close to the  
 552 unit. In order to generalize these results a larger range of  $Da$  numbers should be investigated.

553 In order to estimate the effective thermal conductivity coefficient  $k_e$ , the principle of conservation of  
 554 heat energy can be applied to the whole fractured medium. Neglecting the heat stored in the fractures,



the difference between the heat measured at the inlet and at the outlet must be equal to the heat diffused into the matrix:

$$\rho C_p Q_0 (T_{inj} - T_{out}) = \int_{A_f} k_e \frac{dT_m}{dz} \Big|_{z=w_f/2} dA_f \quad (52)$$

where  $A_f$  is the whole surface area of the whole active fracture network and the gradient of  $T_m$  can be evaluated according to Equation (16). Then the average effective thermal conductivity  $\bar{k}_e$  can be obtained as:

$$\bar{k}_e = \frac{\rho C_p Q_0 (T_{inj} - T_{out})}{\int_{A_f} k_e \frac{dT}{dz} \Big|_{z=w_f/2} dA_f} \quad (53)$$

The average effective thermal conductivity has been estimated for each injection flow rate (Figure 15) and assumes a mean value equal to  $\bar{k}_e = 0.1183 \text{ Wm}^{-1}\text{K}^{-1}$ . The estimated  $\bar{k}_e$  is one order of magnitude lower than the thermal conductivity coefficient reported in the literature (Robertson, 1988). Fractured media have a lower capacity for diffusion as opposed to the Tang's model which has unlimited capacity. There is a solid thermal resistance in the fluid to solid heat transfer processes which depends on the rock – fracture size ratio.

This result is coherent with previous analyses on heat transfer carried out on the same rock sample (Pastore et al. 2015). In this study Pastore et al. (2015) found that the ENM model failed to model the behavior of heat transport in correspondence of parallel branches where the hypothesis of Tang's solution of single fracture embedded in a porous medium having unlimited capacity cannot be considered valid. In parallel branches the observed BTCs are characterized by less retardation of heat propagation as opposed to the simulated BTCs.

## Conclusions

Aquifers offer a possibility of exploiting geothermal energy by withdrawing the heat from groundwater by means of a heat pump and subsequently supplying the water back into the aquifer through an injection well. In order to optimize the efficiency of the heat transfer system and minimize the environmental impacts it is necessary to study the behavior of convective heat transport especially in fractured media, where flow and heat transport processes are not well known.

Laboratory experiments on the observation of mass and heat transport in a fractured rock sample have been carried out in order to analyse the contribution of thermal dispersion in heat propagation



582 processes, the contribution of nonlinear flow dynamics on the enhancement of thermal matrix  
583 diffusion and finally the optimal heat recovery and heat dissipation strategies.

584 The parameters that control mass and heat transport have been estimated using the ENM model based  
585 on Tang's solution.

586 Heat transport shows a very different behavior compared to mass transport. The estimated transport  
587 parameters show differences of several orders of magnitude. Convective thermal velocity is lower  
588 than solute velocity, whereas thermal dispersion is higher than solute dispersion, mass transfer rate  
589 assumes a very low value suggesting that fracture – matrix mass exchange can be neglected. Non -  
590 fickian behavior of observed solute BTCs is mainly due to the presence of the secondary path and  
591 nonlinear flow regime. Contrarily heat transfer rate is comparable with convective thermal velocity  
592 giving rise to a retardation effect on heat propagation in the fracture network.

593 The discrepancies detected in transport parameters are moreover observable through the time moment  
594 and tail character analysis which demonstrate that the dual porosity behavior is more evident in the  
595 thermal BTCs than in the solute BTCs.

596 The dimensionless analysis carried out on the transport parameters proves that as the injection flow  
597 rate increases thermal convection time scale decreases more rapidly than the thermal exchange time  
598 scale, explaining the reason why the relationship  $Q_0 - u_f$  shows a change of slope for  $Da$  lower than  
599 the unit.

600 Thermal dispersion dominates heat transport dynamics, the Peclet number and the product between  
601 Peclet number and Damköhler number is almost always less than the unit.

602 The optimal conditions for thermal exchange in a fracture network have been investigated. The power  
603 exchanged increases in a potential way as  $Da$  increases in the observed range.

604 The rock – fracture size ratio plays an important role in the fluid to solid heat transfer processes. It  
605 represents a key parameter in order to design devices for heat recovery and head dissipation that  
606 exploit the convective heat transport in fractured media. The estimation of the average effective  
607 thermal conductivity coefficient shows that it is not efficient to store thermal energy in rocks with  
608 high fracture density because the fractures are surrounded by a matrix with more limited capacity for  
609 diffusion giving rise to an increase in solid thermal resistance.

610 **References**



- 611 Abate, J. and Ward, W., 2006. A unified Framework for numerically inverting laplace transforms.  
 612 INFORMS Journal of Computing, vol. 18.4 (2006): 408-421.
- 613 Auradou, H., Deazerm G., Boschan, A., Hulin J., Koplik, J., 2006. Flow channeling in a single  
 614 fracture induced by shear displacement. Geothermics 35 575-588.
- 615 Becker, M.W. and Shapiro, A. M., 2003. Interpreting tracer breakthrough tailing from different  
 616 forcedgradient tracer experiment configurations in fractured bedrock. Water Resources Research.  
 617 39(1):1024.
- 618 Bodin, J., Porel, G., Delay, F., Ubertosi, F., Bernard, S. and de Dreuzy, J.R, 2007. Simulation and  
 619 analysis of solute transport in 2D fracture/pipe networks. The SOLFRAC program. Journal of  
 620 Contaminant Hydrology 89 (1-2), 1-28.
- 621 Cherubini C., 2008 A modeling approach for the study of contamination in a fractured aquifer  
 622 Geotechnical and geological engineering 26 (5), 519-533
- 623 Cherubini C, Pastore N, Francani V 2008 Different approaches for the characterization of a fractured  
 624 karst aquifer WSEAS Transactions On Fluid Mechanics 1, 29-35
- 625 Cherubini, C., Giasi, C. I., and Pastore, N., 2009. Application of Modelling for Optimal Localisation  
 626 of Environmental Monitoring Sensors, Proceedings of the Advances in sensor and Interfaces  
 627 (IWASI), Trani, Italy, 222–227.
- 628 Cherubini, C., Pastore, N., 2010a. Modeling contaminant propagation in a fractured and karstic  
 629 aquifer. Fresenius Environmental Bulletin. 19 (9), 1788-1794.
- 630 Cherubini, C., Hsieh, P. A., Tiedeman C. R., 2010b. Modeling the effect of heterogeneity on forced-  
 631 gradient flow tracer tests in heterogeneous aquifers. I Congreso Internacional de Hidrologia de  
 632 Lianuras Azul, Buenos Aires, Argentina – 21 al 24/09/2010.
- 633 Cherubini, C., Pastore, N., 2011. Critical stress scenarios for a coastal aquifer in southeastern Italy.  
 634 Natural Hazards and Earth System Science. 11 (5) p. 1381-1393.
- 635 Cherubini, C., Giasi, C. I., Pastore, N., 2012. Bench scale laboratory tests to analyze non-linear flow  
 636 in fractured media. Hydrology and Earth System Sciences. 16, 2511-2622.
- 637 Cherubini, C., Giasi, C.I., Pastore, N., 2013a. Evidence of non-Darcy flow and non-Fickian transport  
 638 in fractured media at laboratory scale. Hydrology and Earth System Sciences 17, 2599-2611.





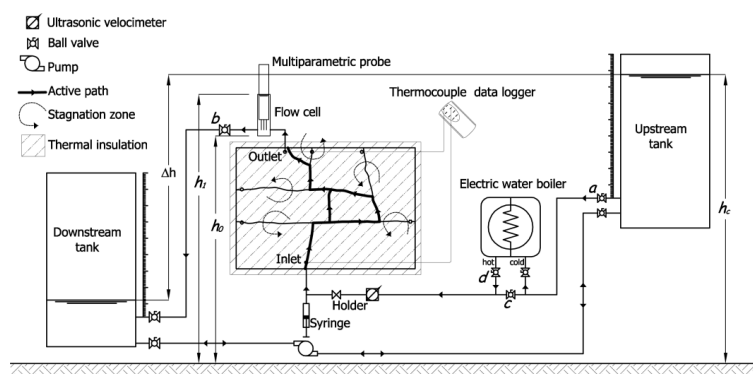
- 639 Cherubini, C., Giasi, C. I., Pastore, N. 2013b. Laboratory tests to analyze solute transport behavior in  
640 fractured media. *Rendiconti Online Società Geologica Italiana*. 24, 55-57.
- 641 Cherubini, C., Giasi, C. I., Pastore, N. 2013c. Un modello fisico di laboratorio per analizzare  
642 dinamiche di flusso e trasporto in un campione di roccia fratturata a scala di banco [A laboratory  
643 physical model to analyse flow and transport processes in fractured rock sample at bench scale level].  
644 *Italian Journal Engineering Geology and Environment*. (1) 19-32.
- 645 Cherubini, C., Giasi, C. I., Pastore, N. 2013d. Fluid flow modeling of a coastal fractured karstic  
646 aquifer by means of a lumped parameter approach. *Environmental Earth Sciences*. 70 (5), 2055-2060.
- 647 Cherubini, C., Giasi, C.I., Pastore, N., 2014. On the reliability of analytical models to predict solute  
648 transport in a fracture network. *Hydrology and Earth System Sciences* 18, 2359-2374.
- 649 De Hoog, F.R., Knight, J.H., Stokes, A.N., 1982. An improved method for numerical inversion of  
650 Laplace transforms. *SIAM J. Sci. Stat. Comput.* 3 (3), 357-366.
- 651 Fahien, R.W., 1983. *Fundamental of Transport Phenomena*. McGraw-Hill, New York.
- 652 Forchheimer, P., 1901. Wasserbewegung durch Boden. *Z. Ver. Dtsch. Ing.* 45, 1781-1788.
- 653 Geiger, S. and Emmanuel, S., 2010. Non-fourier thermal transport in fractured geological media.  
654 *Water Resources Research*, 46, xvii, 26, 27, 168.
- 655 Gisladdottir, V.R., Roubinet, D. & Tartakovsky, D.M. (2016) Particle Methods for Heat Transfer in  
656 Fractured Media *Transp Porous Med* (2016). doi:10.1007/s11242-016-0755-2
- 657 Hao, Y., Fu, P., Carrigan, C. R., 2013. Application of a dual-continuum model for simulation of fluid  
658 flow and heat transfer in fractured geothermal reservoir. *Proceedings, Thirty-Eighth Workshop on*  
659 *Geothermal Reservoir Engineering Stanford University, Stanford, California* 11-12 SGP-TR-198.
- 660 Hasler, A., Gruber, S., Font, M., Dubois, A., 2011. Advective heat transport in frozen rock cleft –  
661 Conceptual model, laboratory experiments and numerical simulation.
- 662 Hawkins, A.J., Becker, M. W., 2012. Measurement of the Spatial Distribution of Heat Exchange in a  
663 Geothermal Analog Bedrock Site Using Fiber Optic Distributed Temperature Sensing.  
664 *PROCEEDINGS, Thirty-Seventh Workshop on Geothermal Reservoir Engineering Stanford*  
665 *University, Stanford, California, January 30 - February 1, 2012 SGP-TR-194*.
- 666 Klepikova, MV, Le Borgne T, Bour, O., Dentz M., Hochreutener R., (2016) Heat as a tracer for  
667 understanding transport processes in fractured media: Theory and field assessment from multiscale  
668 thermal push-pull tracer tests *Water Resources Research* 52 (7), 5442-5457



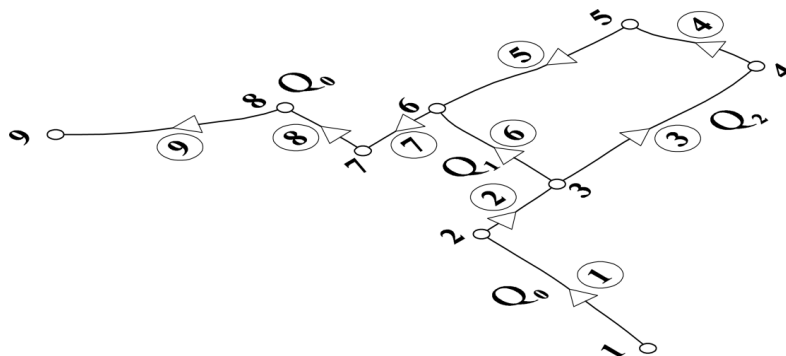
- 669 Kocabas, I., 2005. Geothermal reservoir characterization via thermal injection backflow and interwell  
 670 tracer testing. *Geothermics*, 34:27-46.
- 671 Lu, W., Xiang, Y., 2012. Experiments and sensitivity analyses for heat transfer in a meter-scale  
 672 regularity fracture granite model with water flow. *Journal of Zhejiang University-SCIENCE A*  
 673 (Applied Physics & Engineering). 13(12) 958-968.
- 674 Martinez, A. R., Roubinet, D., Tartakovsky, D.  
 M., 2014. Analytical models of heat conduction in fractured rocks. *J. Geophys. Res. Solid Earth*, 119.
- 675 Masciopinto C, Volpe A, Palmiotta D, Cherubini C A combined PHREEQC-2/parallel fracture model  
 676 for the simulation of laminar/non-laminar flow and contaminant transport with reactions *Journal of*  
 677 *contaminant hydrology* 117 (1), 94-108
- 678 Moonen, P., Sluys, L. J., Carmeliet, J., 2011. A continuous – Discontinuous Approach to simulate heat  
 679 transfer in fractured media. *Transp. Porous Med.* 89 399-419.
- 680 Natarajan, N., Kumar, G. S., 2010. Thermal transport in a coupled sinusoidal fracture-matrix system.  
 681 *International Journal of Engineering Science and Technology* 2(7) 2645-2650.
- 682 Ouyang, X. L., Xu, R. N., Jiang, P. X., 2014. Effective solid-to-fluid heat transfer coefficient in egs  
 683 reservoirs. *Proceedings of the 5<sup>th</sup> International Conference on porous Media and its Applications in*  
 684 *Science and Engineering ICPM5 June 22-27, 2014, Kona, Hawaii.*
- 685 Pastore N., Cherubini C., Giasi C. I., Allegretti N. M., Redondo J. M., Tarquis A. M. (2015)  
 686 *Experimental study of heat transport in fractured network Energy Procedia* 76 ( 2015 ) 273 – 281
- 687 Read T, Bour, O., Bense, V., Le Borgne, T., Goderniaux, P., Klepikova, M. V., Hochreutener, R.,  
 688 Lavenant, N., Boshero, V., 2013. Characterizing groundwater flow and heat transport in fractured  
 689 rock using fiber-optic distributed temperature sensing. *Geophysical research letters*, 40 1-5.
- 690 Robertson, E.C., 1988. *Thermal Properties of Rocks*. United States Department of the Interior  
 691 Geological Survey Open-File Report 88-441. Reston, Virginia.
- 692 Shook, G. M., 2001. Predicting thermal breakthrough in heterogeneous media from tracer tests.  
 693 *Geothermics* 30(6), 573-580.
- 694 Tang, D.H., Frind, E.O., Sudicky, E.A., 1981. Contaminant transport in fractured porous media:  
 695 analytical solutions for a single fractures. *Water Resources Research*, Vol. 17, No 3, pp. 555-564.
- 696 Tsang, C. F. and Neretnieks, I., 1998. Flow channeling in heterogeneous fractured rocks. *Reviews of*  
 697 *Geophysics*, 36 257-298.



700



702 **Figure 1. Schematic diagram of the experimental setup.**



704 **Figure 2. Two dimensional pipe network conceptualization of the fracture network.**

27



4.074	15.88	÷	16.02	1.19	÷	1.21	2.89	÷	2.94	0.0048	0.9979
4.087	15.07	÷	15.20	1.11	÷	1.13	3.75	÷	3.83	0.0045	0.9976
4.132	14.71	÷	14.82	1.08	÷	1.09	2.93	÷	2.98	0.0028	0.9985
4.354	15.63	÷	15.77	1.14	÷	1.16	3.24	÷	3.30	0.0052	0.9979
4.529	17.05	÷	17.21	1.30	÷	1.32	2.88	÷	2.94	0.0055	0.9978
5.852	19.26	÷	19.38	1.44	÷	1.46	4.21	÷	4.25	0.0042	0.9983
5.895	19.38	÷	19.54	1.37	÷	1.39	3.77	÷	3.82	0.0058	0.9981
6.168	18.98	÷	19.17	1.36	÷	1.39	2.87	÷	2.92	0.0091	0.9973
7.076	20.64	÷	20.86	1.36	÷	1.39	3.33	÷	3.39	0.0123	0.9963
7.620	20.47	÷	20.75	1.52	÷	1.55	2.33	÷	2.39	0.0180	0.9951
7.983	21.33	÷	21.58	1.61	÷	1.64	2.92	÷	2.98	0.0137	0.9965
8.345	21.71	÷	21.97	1.65	÷	1.68	2.81	÷	2.86	0.0136	0.9964

Table 1. Estimated values of parameters, RMSE, and determination coefficient  $r^2$  for ENM with Tang's solution at different injection flow rates for mass transport.

$Q_0$ ( $\text{m}^3\text{s}^{-1}$ ) $\times 10^{-6}$	$u_f$ ( $\text{ms}^{-1}$ ) $\times 10^{-3}$	$D_f$ ( $\text{ms}^{-2}$ ) $\times 10^{-3}$	$\alpha$ ( $\text{s}^{-1}$ ) $\times 10^{-3}$	RMSE	$r^2$
1.835	2.20 ÷ 2.91	1.91 ÷ 1.95	6.27 ÷ 6.59	0.0065	0.9997
2.325	1.74 ÷ 2.73	1.82 ÷ 1.91	5.39 ÷ 9.26	0.0098	0.9992
2.462	0.35 ÷ 0.52	2.42 ÷ 2.57	2.25 ÷ 2.33	0.0138	0.9984
2.605	0.44 ÷ 0.54	2.33 ÷ 2.40	0.74 ÷ 0.77	0.0073	0.9995
2.680	2.18 ÷ 2.95	1.77 ÷ 1.83	5.68 ÷ 8.31	0.0030	0.9998
2.800	0.36 ÷ 0.79	2.53 ÷ 2.68	3.54 ÷ 3.72	0.0213	0.9982
2.847	1.73 ÷ 3.16	1.98 ÷ 2.06	4.95 ÷ 13.45	0.0283	0.9978
3.003	2.34 ÷ 2.87	2.24 ÷ 2.32	5.33 ÷ 6.55	0.0033	0.9998
3.998	2.56 ÷ 2.75	6.63 ÷ 6.80	2.05 ÷ 2.11	0.0150	0.9993
4.030	2.60 ÷ 2.83	7.18 ÷ 7.36	1.42 ÷ 1.52	0.0147	0.9993
4.217	3.85 ÷ 4.56	8.92 ÷ 9.29	4.86 ÷ 5.77	0.0228	0.9945
4.225	2.43 ÷ 2.64	7.53 ÷ 7.84	1.64 ÷ 1.80	0.0251	0.9987
4.471	2.30 ÷ 3.13	9.18 ÷ 9.50	1.06 ÷ 1.33	0.1115	0.9957
5.837	3.51 ÷ 4.13	4.95 ÷ 5.36	0.61 ÷ 0.79	0.2360	0.9872
5.880	2.71 ÷ 3.10	4.23 ÷ 4.60	0.04 ÷ 0.05	0.1997	0.9926
6.445	4.71 ÷ 5.12	6.18 ÷ 6.81	1.49 ÷ 1.54	0.2156	0.9863
7.056	8.15 ÷ 8.46	10.05 ÷ 10.74	5.63 ÷ 6.00	0.0694	0.9951
7.959	9.64 ÷ 10.11	18.40 ÷ 19.47	10.92 ÷ 11.55	0.0662	0.9971
8.971	13.40 ÷ 13.79	24.57 ÷ 25.82	15.35 ÷ 15.85	0.0303	0.9985
12.364	11.01 ÷ 11.67	21.97 ÷ 22.63	5.23 ÷ 5.25	0.0631	0.9939
12.595	13.71 ÷ 14.26	26.65 ÷ 27.61	9.26 ÷ 9.41	0.0426	0.9955

Table 2. Estimated values of parameters, RMSE, and determination coefficient  $r^2$  for ENM with Tang's solution at different injection flow rates for heat transport.

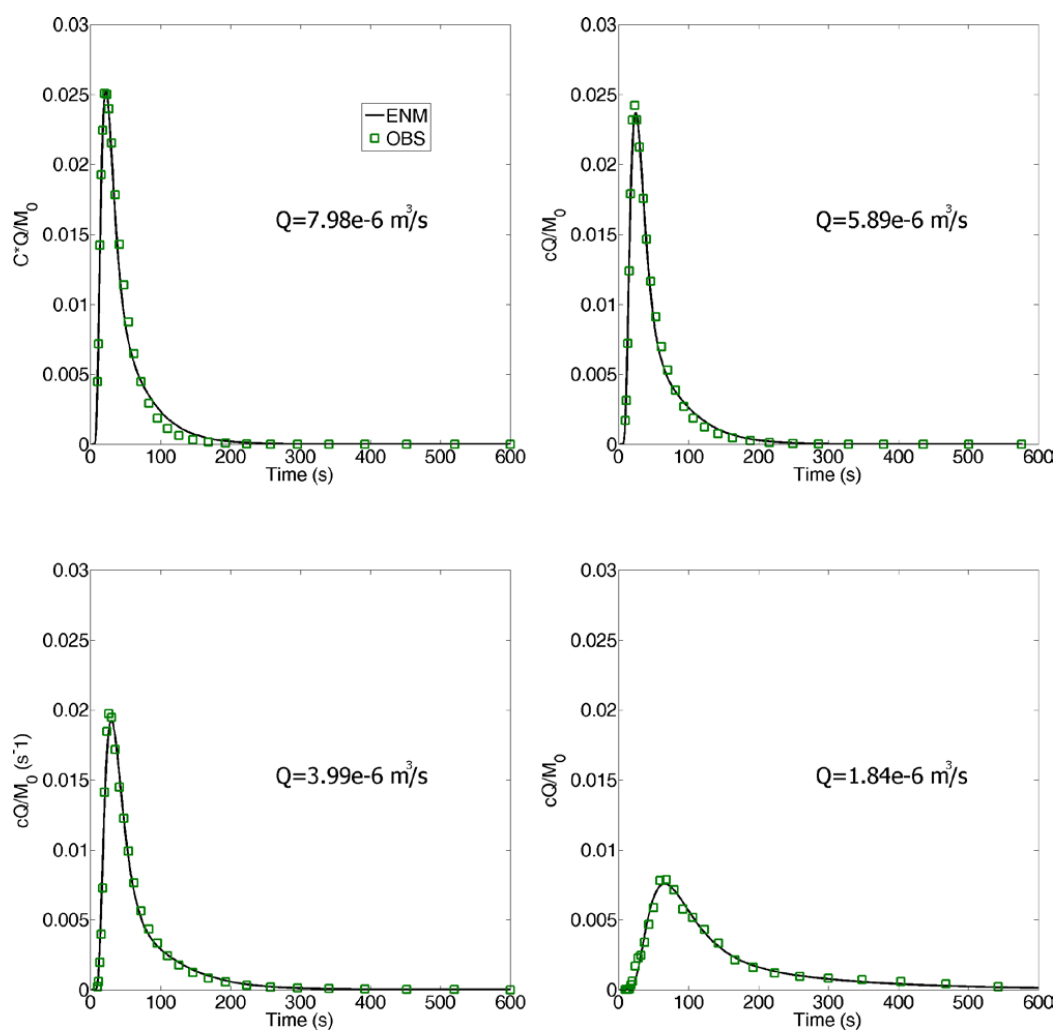


Figure 3. Fitting of BTCs at different injection flow rates using ENM with Tang's solution for mass transport.

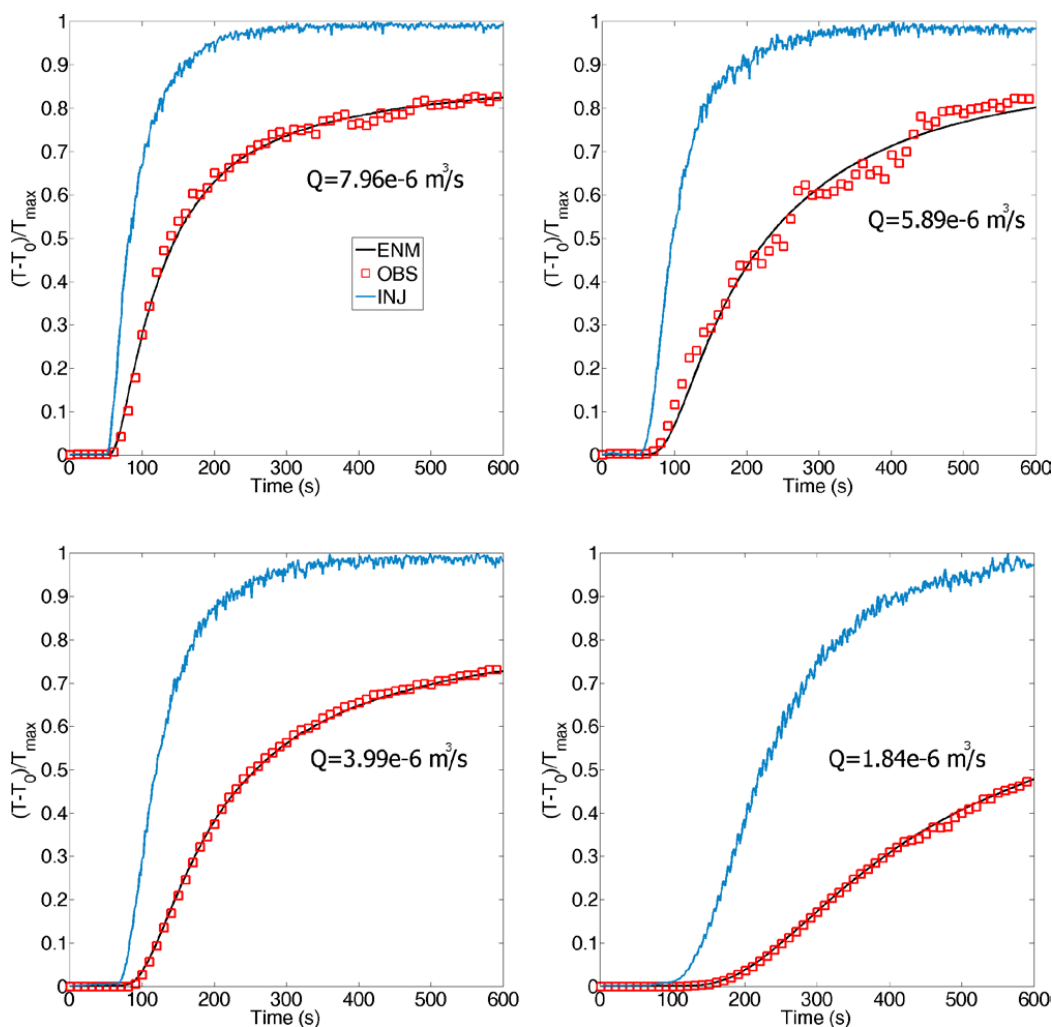
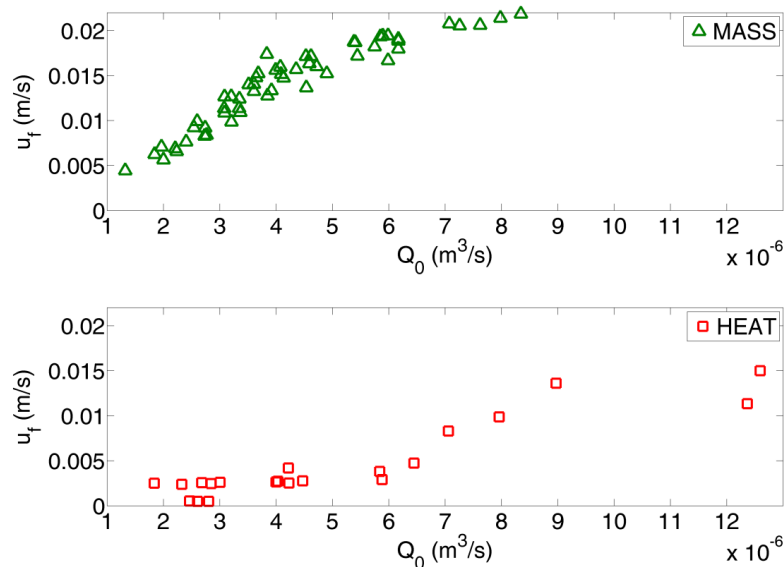
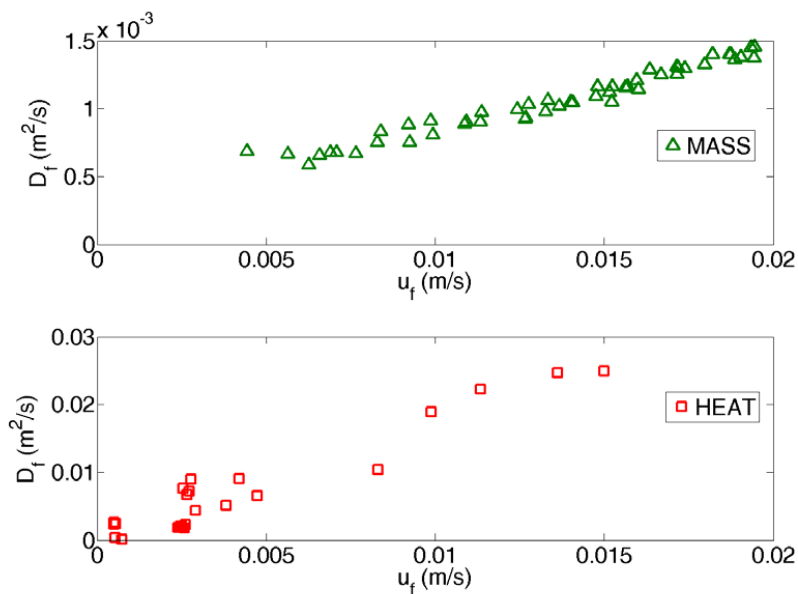


Figure 4. Fitting of BTCs at different injection flow rates using ENM with Tang's solution for heat transport.



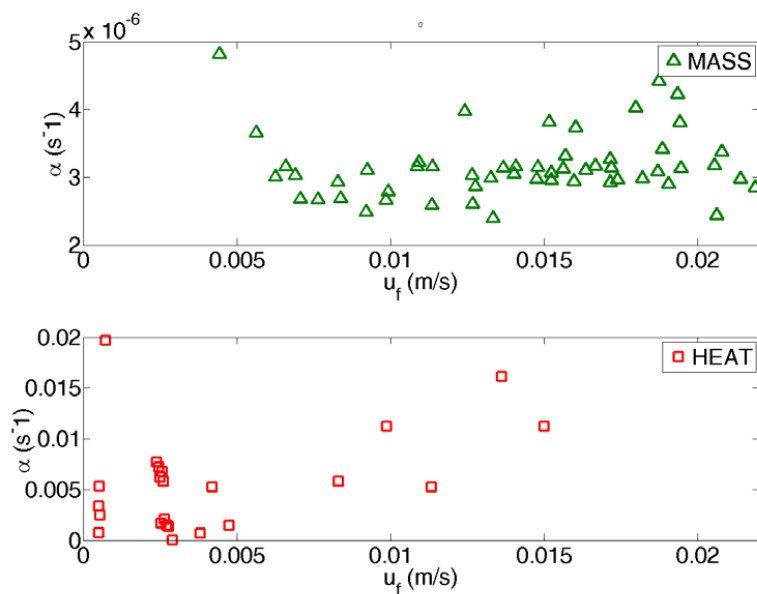
716

717 **Figure 5. Velocity  $u_f$  (m s<sup>-1</sup>) as function of the injection flow rate  $Q_0$  (m<sup>3</sup>s<sup>-1</sup>) for ENM with Tang's solution for both mass and**  
 718 **heat transport.**



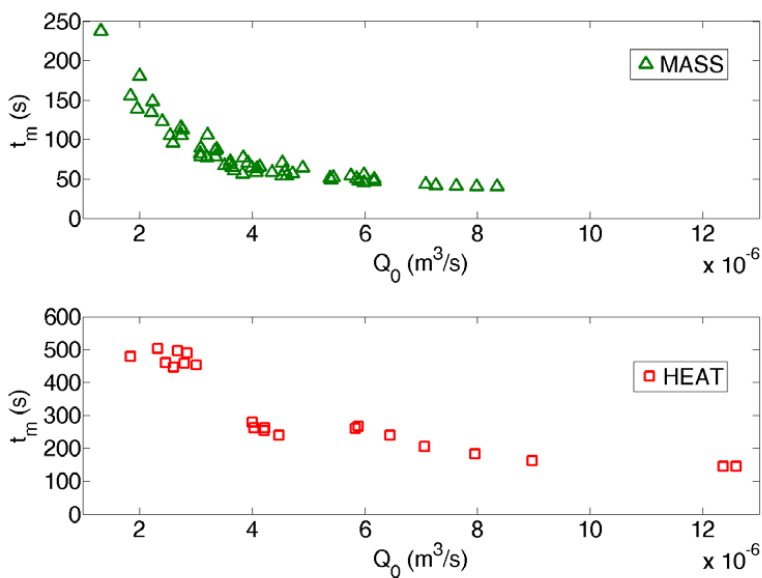
719

720 **Figure 6. Dispersion  $D_f$  (m s<sup>-2</sup>) as function of velocity  $u_f$  (m s<sup>-1</sup>) for ENM with Tang's solution for both mass and**



721

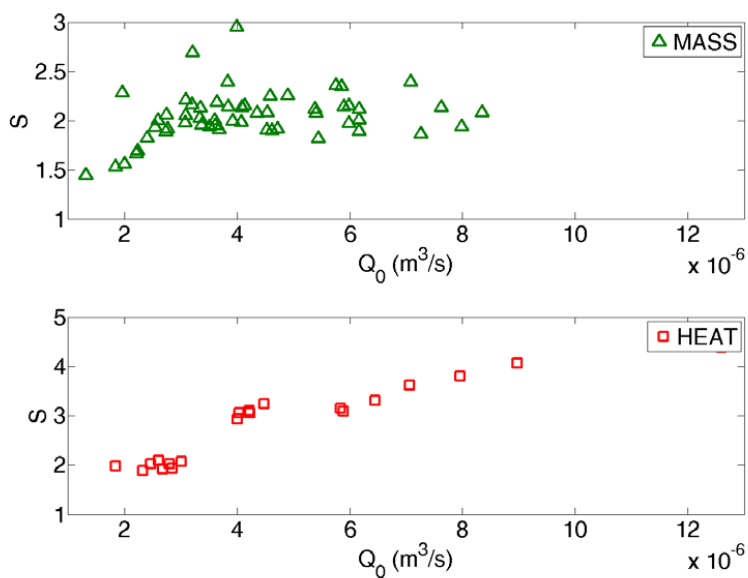
722 **Figure 7. Transfer coefficient  $\alpha$  ( $\text{s}^{-1}$ ) as function of velocity  $u_f$  ( $\text{ms}^{-1}$ ) for both mass and heat transport.**



723

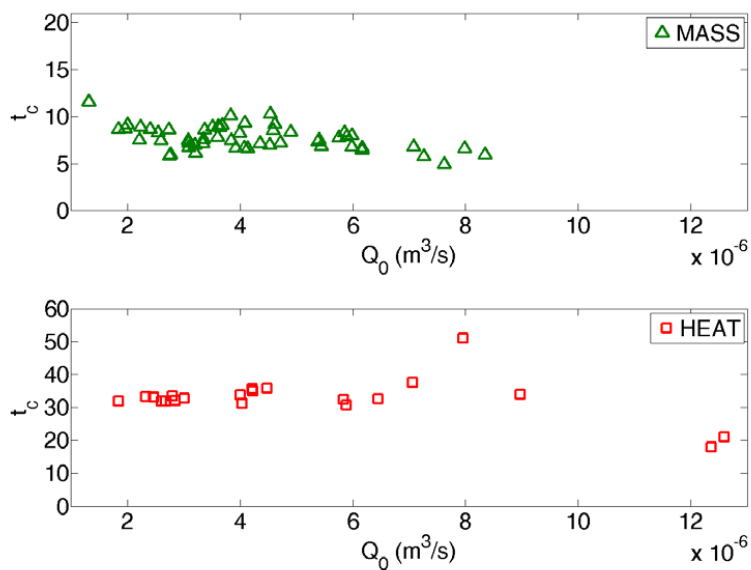
724 **Figure 8. Mean travel time  $t_m$  (s) as function of injection flow rate for both mass and heat transport.**





725

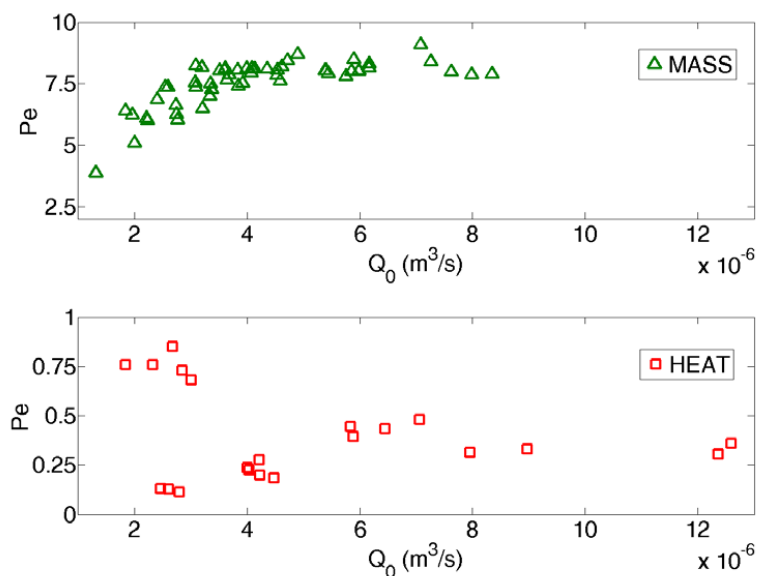
726 **Figure 9. Skewness as function of injection flow rate for both mass and heat transport.**



727

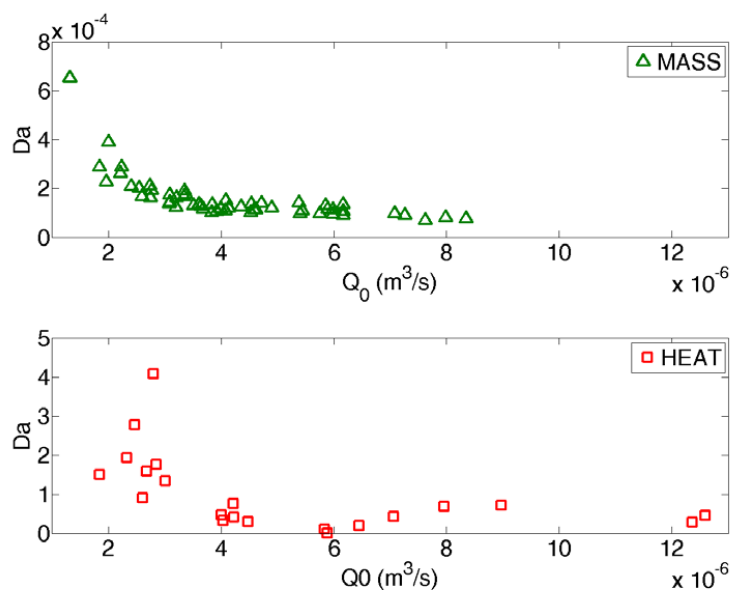
728 **Figure 10. Tailing character  $t_c$  as function of injection flow rate for both mass and heat transport.**

729



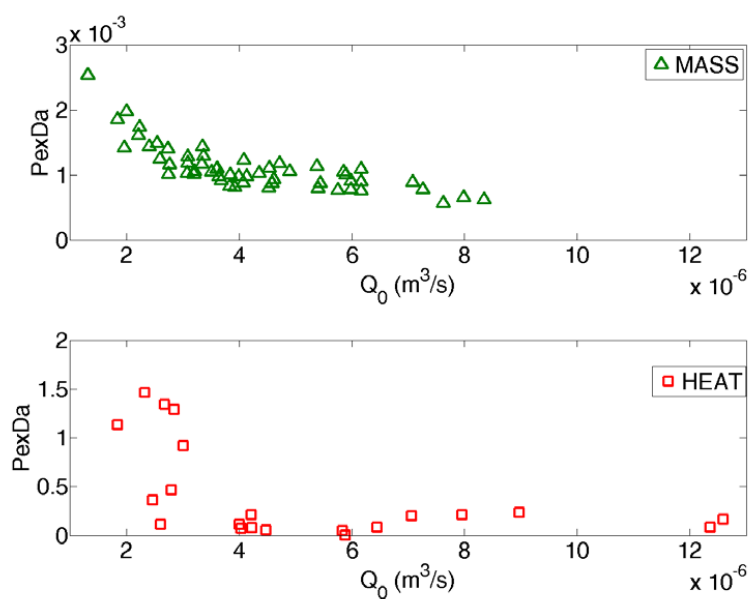
730

731 **Figure 11. Peclet number as function of injection flow rate  $Q_0$  (m<sup>3</sup>s<sup>-1</sup>) for both mass and heat transport.**



732

733 **Figure 12. Da number as function of injection flow rate  $Q_0$  (m<sup>3</sup>s<sup>-1</sup>) for both mass and heat transport.**



734

735 **Figure 13. PexDa number as function of injection flow rate  $Q_0$  (m<sup>3</sup>s<sup>-1</sup>) for both mass and heat transport.**

736

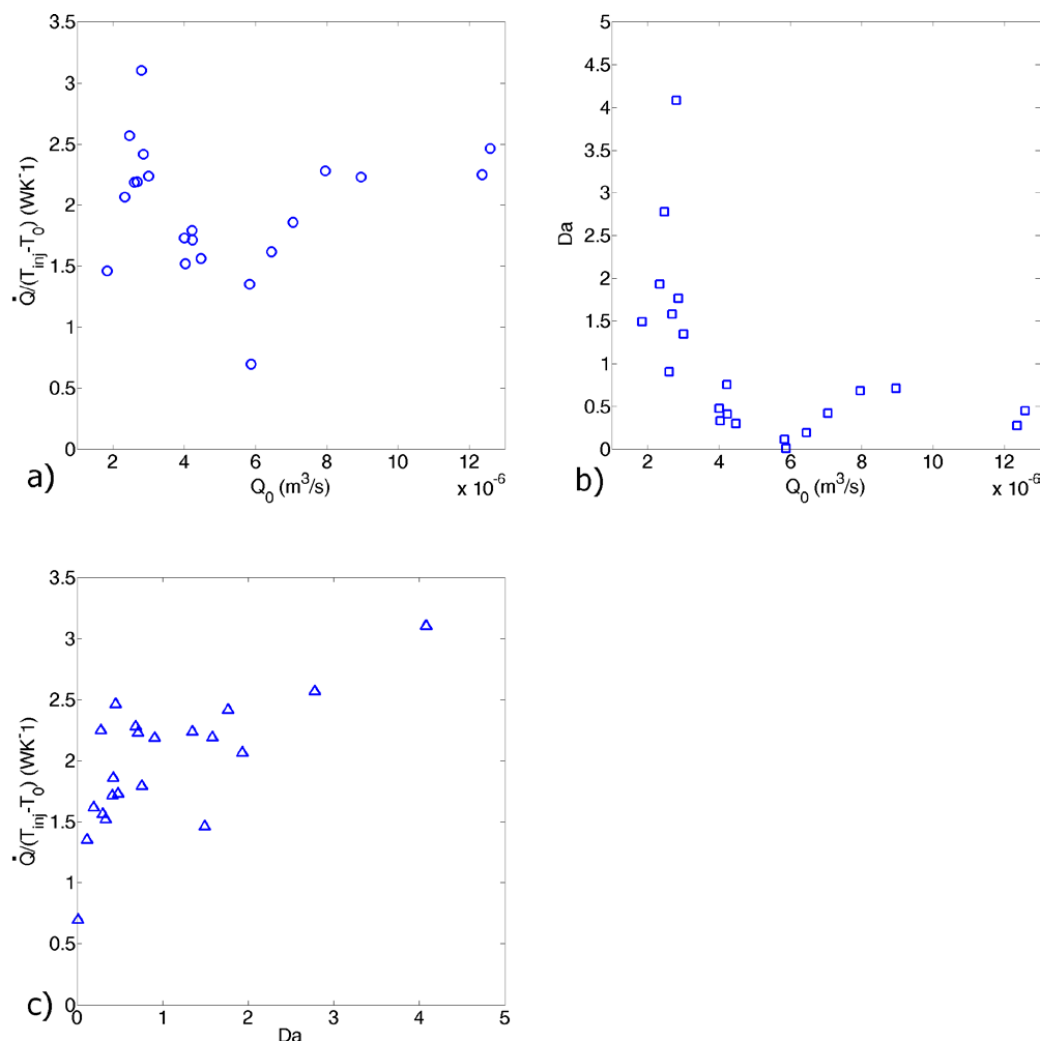
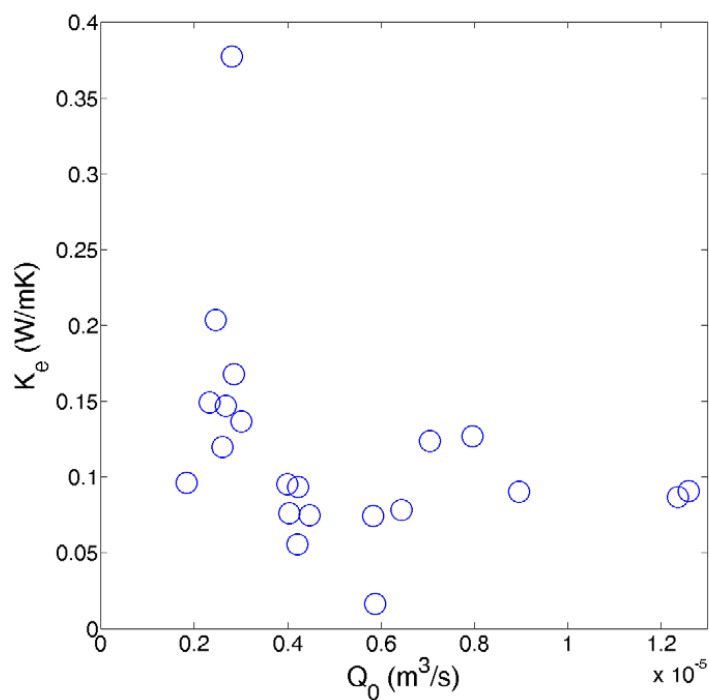


Figure 14. Heat power exchanged per difference temperature unit  $\dot{Q}/(T_{inj}-T_0)$  as function of injection flow rate  $Q_0$  (m<sup>3</sup>s<sup>-1</sup>) (a), Damköhler number  $Da$  as function of injection flow rate (b), power exchanged per difference temperature unit as function of Damköhler number (c).



742

743 **Figure 15. Effective thermal conductivity  $k_e$  ( $\text{Wm}^{-1}\text{K}^{-1}$ ) as function of injection flow rate  $Q_0$  ( $\text{m}^3\text{s}^{-1}$ ).**